

Epitaxial Growth of Rutile GeO₂ via MOCVD

Imteaz Rahaman¹, Bobby Duersch², Hunter D. Ellis¹, Michael A. Scarpulla^{1,3}, and Kai Fu^{1, a)}

¹*Department of Electrical and Computer Engineering, The University of Utah, Salt Lake City, UT 84112, USA*

²*Electron Microscopy and Surface Analysis Laboratory, The University of Utah, Salt Lake City, UT 84112, USA*

³*Department of Materials Science and Engineering, The University of Utah, Salt Lake City, UT 84112, USA*

Abstract

Rutile Germanium Dioxide (r-GeO₂) has been identified as an ultrawide bandgap (UWBG) semiconductor recently, featuring a bandgap of 4.68 eV—comparable to Ga₂O₃—but offering bipolar dopability, higher electron mobility, higher thermal conductivity, and higher Baliga's figure of merit (BFOM). These superior properties position GeO₂ as a promising material for various semiconductor applications. However, the epitaxial growth of r-GeO₂, particularly in its most advantageous rutile polymorph, is still at an early stage. This work explores the growth of r-GeO₂ using metal-organic chemical vapor deposition (MOCVD) on an r-TiO₂ (001) substrate, utilizing tetraethyl germane (TEGe) as the precursor. Our investigations reveal that higher growth temperatures significantly enhance crystalline quality, achieving a full width at half maximum (FWHM) of 0.181° at 925 °C, compared to 0.54° at 840 °C and amorphous structures at 725 °C. Additionally, we found that longer growth durations increase surface roughness due to the formation of faceted crystals. Meanwhile, adjusting the susceptor rotation speed from 300 RPM to 170 RPM plays a crucial role in optimizing crystalline quality, effectively reducing surface roughness by approximately 15 times. This study offers a foundational guide for optimizing MOCVD growth conditions of r-GeO₂ films, emphasizing the crucial need for precise control over

deposition temperature and rotation speed to enhance adatom mobility and effectively minimize the boundary layer thickness.

^{a)} Author to whom correspondence should be addressed. Electronic mail: kai.fu@utah.edu

I. Introduction

Wide bandgap (WBG) and ultra-wide bandgap (UWBG) semiconductors, such as SiC (3.2 eV),¹ GaN (3.39 eV),² AlGaN (3.4-6 eV),³ β -Ga₂O₃ (4.5-4.8 eV),⁴ and diamond (5.47 eV)⁵, have undergone extensive exploration for applications in power electronics, extreme environment electronics, gas sensors, and UV detectors due to their larger breakdown strength, increased power density, and reduced energy loss.⁶⁻⁸ β -Ga₂O₃ stands out in high-power device applications, evident in Baliga's figure of merit comparison with Si (3000 \times), SiC (10 \times), and GaN (4 \times).⁹ However, β -Ga₂O₃ has difficulty in effective p-type conductivity and poor thermal conductivity.¹⁰⁻¹² For AlGaN, acceptor activation efficiency, and hole mobility are suppressed by increasing the Al content.^{13,14} Diamond suffers from a lack of industrially applicable substrates and effective dopants due to high ionization energies.¹⁵ The advancement of all current UWBG semiconductors is hindered by challenges such as limited wafer sizes and difficulties in doping. Recently, r-GeO₂ has emerged as a novel UWBG semiconductor due to its remarkable physical properties and potential to address these challenges. It has a bandgap of 4.44 to 4.68 eV¹⁶⁻¹⁸ and a high predicted electron mobility [244 cm²/Vs ($\perp\vec{C}$) and 377 cm²/V \cdot s ($\parallel\vec{C}$)]¹⁹, giving it a high n-type Baliga figure of merit (27,000–35,000 $\times 10^6$ V² Ω^{-1} cm⁻²).²⁰ Moreover, the thermal conductivity of r-GeO₂ is 37 and 58 W/m \cdot K along the *a* and *c* directions, respectively, with a measurement of 51 Wm⁻¹K⁻¹, roughly twice that of Ga₂O₃.²¹ Theoretical studies suggest that r-GeO₂ can be ambipolar doped and has relatively high hole mobility [27 cm²/Vs ($\perp\vec{C}$) and 29 ($\parallel\vec{C}$)], indicating its potential for p-n

homojunction and other bipolar devices.^{17,19,22} Furthermore, bulk r-GeO₂ can be synthesized like Ga₂O₃ and GeO₂, making large wafer sizes of GeO₂ available soon.^{23–25}

In 2020, Chae *et al.* epitaxially stabilized r-GeO₂ thin films on R-plane sapphire substrates using a (Sn,Ge)O₂ buffer layer via molecular beam epitaxy (MBE).²⁶ Their work revealed a narrow growth window and a low growth rate of 10 nm/h for r-GeO₂. In 2021, Takane *et al.* established a growth process via mist chemical vapor deposition (mist CVD), achieving growth rates of 1.2–1.7 μm/h on (001) r-TiO₂ substrates.²⁷ Deng *et al.* used pulsed laser deposition to synthesize GeO₂ films, facing significant challenges in stabilizing the rutile phase due to the presence of metastable glass forms.²⁸ In 2024, Rahaman *et al.* reported the growth of polycrystalline GeO₂ on R-plane and C-plane sapphires by metalorganic chemical vapor deposition (MOCVD).²⁹ Despite these advances in thin-film r-GeO₂ growth, as far as we know, there is no report so far of the successful growth of r-GeO₂ by MOCVD which remains the preferred method for large-scale wafer epitaxy in mass production.

In this study, we report the successful growth of r-GeO₂ on (001) TiO₂ substrates using MOCVD. We have investigated the impact of growth parameters—temperature (725 °C to 925 °C), duration (90 to 180 minutes), and rotation speed (170 RPM to 300 RPM)—on the epitaxial film quality. The films were thoroughly analyzed using X-ray Diffraction (XRD), Scanning Electron Microscopy (SEM), X-ray Reflectivity (XRR), Energy Dispersive X-ray Spectroscopy (EDX), Reciprocal Space Mapping (RSM), and Atomic Force Microscopy (AFM). Our results have shown that high-quality film can be obtained at a high temperature of 925 °C in this work, with a 170 RPM rotation speed, where the full width at half maximum (FWHM) is 0.181° (651.6

arcsec). Moreover, this condition can result in a relatively low surface RMS roughness of 13 nm. This research offers a guide for growing r-GeO₂ single crystal films by MOCVD.

II. Experimental Details

The growth of GeO₂ films was carried out in an Agilis MOCVD system, developed by Agnitron Technology. The r-TiO₂ was selected as the substrate due to its relatively small lattice mismatch and low strain with GeO₂.^{27,30} The growth temperature varied from 725°C to 925°C while maintaining a constant chamber pressure of 80 Torr. TEGe and pure oxygen (O₂) were used as precursors, with argon (Ar) serving as both the carrier and shroud gas. The oxygen flow rate was set at 2000 SCCM, the argon shroud gas flow rate at 1250 SCCM, and the TEGe precursor flow rate at 160 SCCM. The susceptor rotation speeds tested were 300 RPM and 170 RPM, to assess the effects of it on film quality. Prior to loading into the MOCVD chamber, the TiO₂ substrates were cleaned using a piranha solution (H₂SO₄ = 3:1), followed by successive cleaning with acetone, isopropanol, and deionized water. A comprehensive list of the growth parameters and their corresponding sample IDs is presented in Table I.

Table I. Summary of GeO₂ films grown at different growth conditions, including growth temperature, chamber pressure, TEGe precursor flow rate, O₂ flow rate, shroud gate flow rate, and susceptor rotation speed.

Sample ID	Temperature (°C)	Pressure (Torr)	TEGe Precursor Flow rate (SCCM)	Oxygen Flow rate (SCCM)	Shroud gas Flow rate (SCCM)	Rotation speed (RPM)	Growth duration (min)
T19	725	80	160	2000	1250	300	90
T23	840	80	160	2000	1250	300	90
T22	925	80	160	2000	1250	300	180
T25	925	80	160	2000	1250	300	90
T26	925	80	160	2000	1250	170	180

The structural properties of the GeO₂ thin film were analyzed using a Bruker D8 Discover High-resolution XRD (HRXRD) with a 1.5406 Å Cu Kα₁ source with a hybrid monochromator. The surface morphology of the films was examined with the FEI TENE0 SEM and the Bruker Dimension ICON AFM.

III. Results and Discussion

The tetragonal crystal structure of the r-GeO₂ is shown in Fig 1 (a). It is thermodynamically the most stable phase of GeO₂ with the *a* and *c* lattice parameters of 4.40656 Å and 2.86186 Å, respectively, and not water-soluble.³¹ Figure 1(b) depicts the breakdown electric field as a function of the energy bandgap in semiconductors ($E_c \sim E_g^{2.3}$), with GeO₂ included.

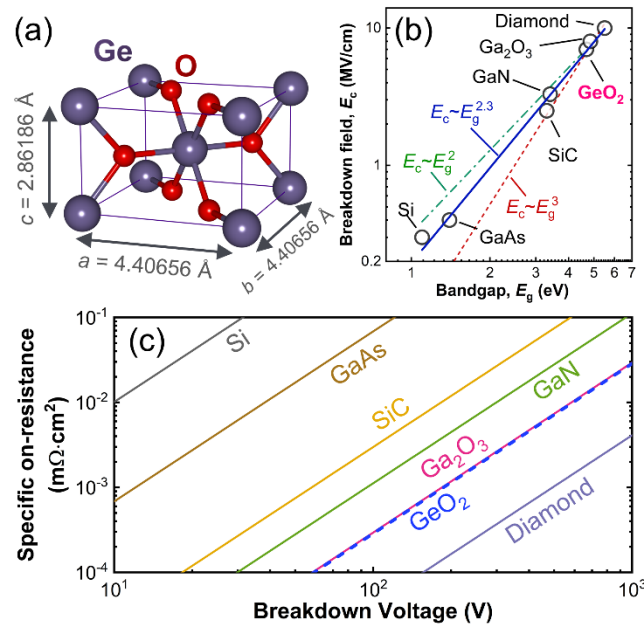


Fig 1. (a) Tetragonal crystal structure of r-GeO₂, showing the lattice parameters with germanium (Ge) atoms in red and oxygen (O) atoms in purple. (b) Breakdown electric field (E_c) vs energy bandgap (E_g) for various semiconductor materials. (c) Specific on-resistance of the semiconductors as a function of breakdown voltage based on the BFOM values in Table II.

The plot reveals a clear linear trend of their relationship on a logarithmic scale. Figure 1(c) presents the BFOM of GeO₂ alongside other semiconductors, revealing that GeO₂ exhibits a slightly higher BFOM than Ga₂O₃. The calculation of BFOM is highly sensitive to material properties, resulting in variations in the reported values since researchers use different material properties based on their understanding and the quality of the materials continues to advance. The material properties of GeO₂ and other semiconductors are listed in Table I based on reported data^{32–34} for comparison.

Table II. Material properties of GeO₂ and other semiconductors.

Properties	Si	GaAs	4H-SiC	GaN	GeO ₂	Ga ₂ O ₃	Diamond
Bandgap, E_g (eV)	1.1	1.4	3.3	3.4	4.68	4.85	5.5
Breakdown field, E_c (MVcm ⁻¹)	0.3	0.4	2.5	3.3	7	8	10
Electron mobility, μ (cm ² V ⁻¹ s ⁻¹)	1400	8000	1000	1250	377	300	2000
Relative dielectric constant, ϵ	11.8	12.9	9.7	9	12.2	10	5.5
Thermal conductivity, λ (Wcm ⁻¹ K ⁻¹)	1.5	0.5	4.9	2.3	0.51	0.1-0.3	20
BFOM, $\epsilon\mu E_c^3$ (GWcm ⁻²)	0.04	0.58	13.42	35.80	139.68	136.00	973.96

The crystal quality of the GeO₂ films is characterized by HRXRD scanning shown in Fig. 2 (a-c), illustrating the variations in film properties across a range of experimental conditions. It can be seen that the GeO₂ film is amorphous for a growth temperature of 725 °C (Fig. 2(a), sample T-19). However, when the growth temperature reaches 840 °C, the film begins to exhibit epitaxial growth of crystalline r-GeO₂, indicated by a broad peak (65.14°) in the XRD pattern (Fig. 2(a), sample T-23). This peak sharpens significantly for samples with a growth temperature increasing to 925 °C (Fig. 2(a), sample T-25). This change can be attributed to the enhanced mobility of adatoms at elevated temperatures, which, at lower temperatures, is insufficient to facilitate film crystallization.²⁶ Additionally, Takane *et al.* have highlighted the critical need to balance adsorption and desorption for successful crystalline film formation.²⁷ This equilibrium also aids in determining whether the deposited layer will be amorphous or crystalline by comparing the net mass addition rate (growth rate) to adatom diffusivity.

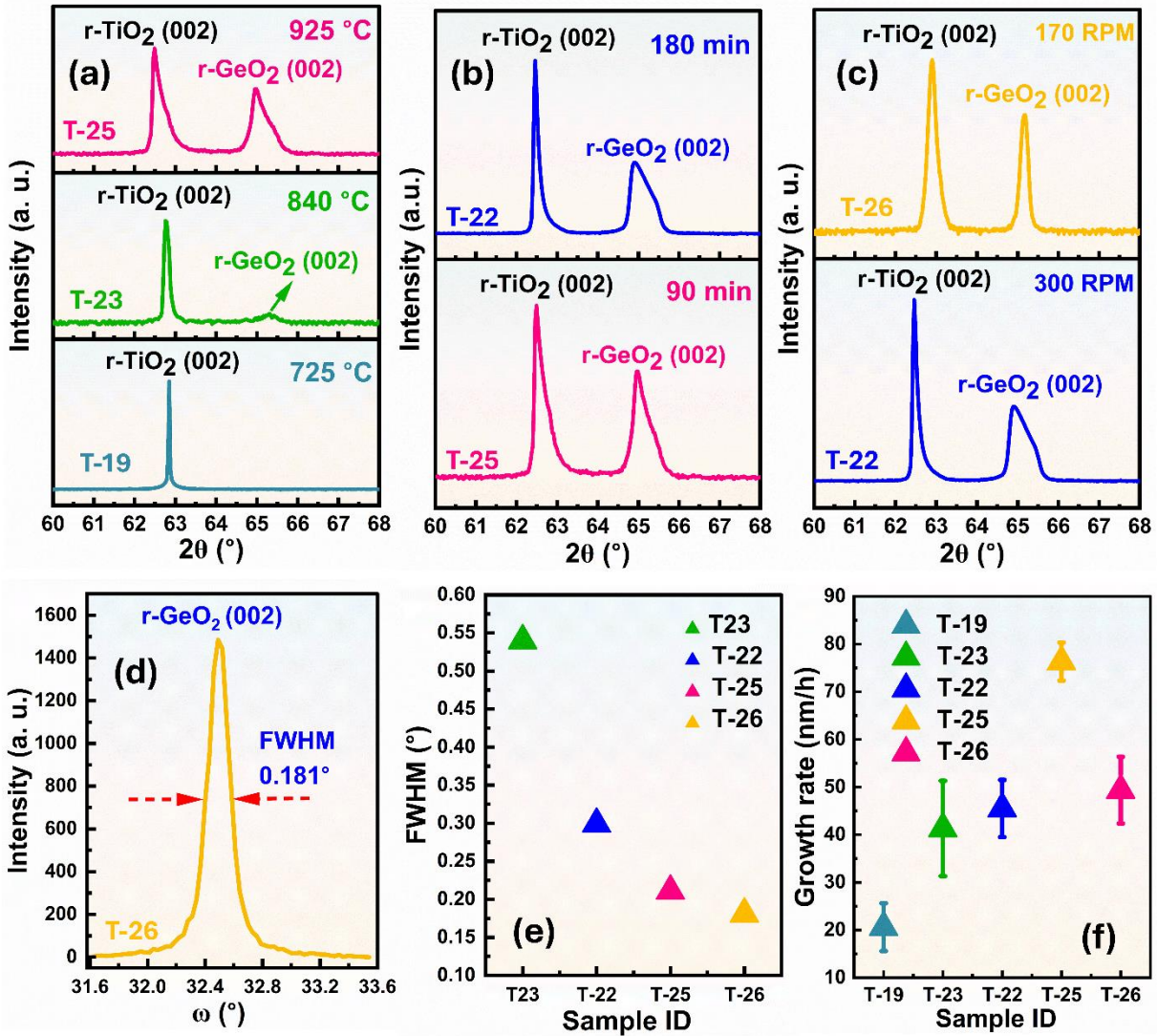


FIG. 2. The HRXRD θ - 2θ data from epitaxial r-GeO₂ Films on (001) r-TiO₂ Substrates as a function of (a) growth temperatures with rotation speed of 300 RPM and growth duration 90 min, (b) different growth durations at 925 °C with rotation speed of 300 RPM, and (c) various susceptor rotation speeds at 925 °C with a growth duration of 180 min. (d) XRD rocking curve of the r-GeO₂ (002) peak from sample ID T-26. (e) Comparative FWHM of all samples. (f) Growth rates of the samples with different growth conditions. Thickness measurements were conducted by XRR.

For samples with an extended growth period of up to 180 minutes (sample T-22), the XRD peak broadens with an FWHM of 0.299° , compared to 0.211° of sample T-25 with a shorter growth

time. Since our previous work has shown that the rotation speed affects the film quality²⁹, the susceptor rotation speed was also investigated by reducing it from 300 RPM to 170 RPM, maintaining a 180-minute growth period at 925 °C. This adjustment resulted in a sharper XRD peak for r-GeO₂ film and an improved FWHM of 0.181° (651.6 arcsec), as shown in the rocking curve for sample T-26 in Fig. 2(d). Figure 2(e) summarizes the FWHM for all the samples. The growth rates of all the samples at different growth conditions are shown in Fig. 2(f), revealing the lowest growth rate for samples with a growth temperature of 725 °C (T-19) and increased growth rates for higher temperatures. The sample T-26, with the best crystalline quality in this study, shows a growth rate of about $\sim 49.36 \pm 7$ nm/h, which is slightly smaller than the film grown with a higher rotation speed (T-25). The error bar of growth rate was set using Leptos 7.14 software by estimating the film thickness at different angles from the fringe peaks in the Fast Fourier Transform (FFT) analysis.

Figure 3 presents symmetrical and asymmetrical RSMs for the sample T-25 and T-26. The symmetric reflections in Figure 3(a) and (c) align precisely with the corresponding substrate peaks in the q_{\parallel} - direction, indicating minimal tilt of the c -axis of the film relative to that of the substrate. The presence of $K\alpha_1$ splitting in the film reflections and minimal broadening in the q_{\perp} - direction in Fig. 3(a) for sample T-26 points to the high quality of the film, in contrast to the observations in Fig. 3(c) for Sample T-25. Furthermore, the higher broadening observed in the q_{\parallel} - direction in Fig. 3(a) suggests slightly increased mosaicity.

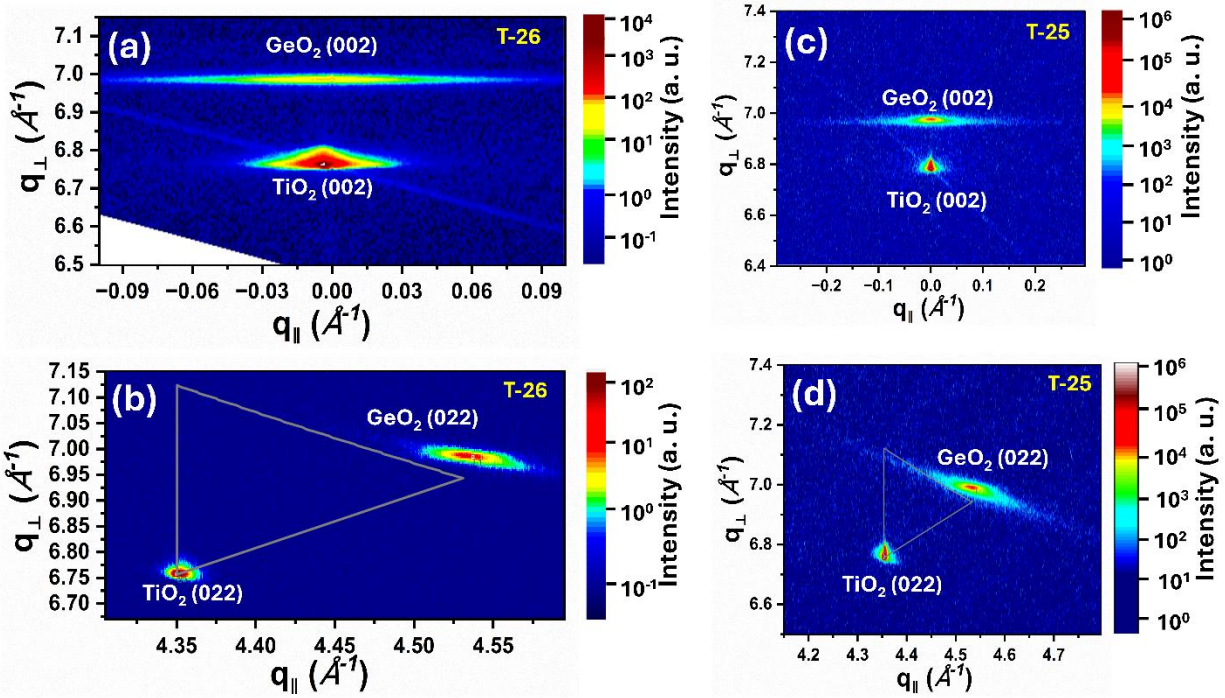


FIG. 3. Reciprocal space mappings of TiO_2 substrates and $r\text{-GeO}_2$ films: (a) symmetrical (002) reflections for sample T-26, (b) asymmetrical (022) reflections for sample T-26, (c) symmetrical (002) reflections for sample T-25, and (d) asymmetrical (022) reflections for sample T-25. Data for these RSM plots were generated and analyzed using Leptos 7.14 software.

Additionally, the (022) reflections of Fig. 3(b) exhibit low broadening with $K\alpha_1$ splitting in the q_{\perp} -direction, indicating less elongation in regions with coherent scattering laterally. Nevertheless, the presence of the (022) reflections in their correct positions relative to the substrate reflections, along with similar q_{\parallel} values, confirms the epitaxial growth of the thin film. However, despite these similarities, the q_{\parallel} and q_{\perp} values of these reflections do not align with the corresponding substrate peak positions, as marked by the triangles in Fig. 3(b) and (d). The triangle is automatically generated by the Leptos 7.14 software during our RSM image processing to facilitate the strain analysis of the film. This discrepancy indicates that the (022) reflections of the film are shifted away from the substrate peaks. We have depicted the strain of all the films in Table III.

Table III. Characteristics of all the samples estimated from XRD data.

Sample ID	$2\theta_{r-GeO_2}$ (°)	Lattice parameter, c_{r-GeO_2} (Å)	Strain of c -axis (%)
T-23	65.31060	2.8552	-0.23 (compressive)
T-22	64.90787	2.8709	+0.32 (tensile)
T-25	64.96467	2.8687	+0.24 (tensile)
T-26	65.17339	2.8605	-0.048 (compressive)

The lattice constant c is measured by the following equation ³⁵-

$$\frac{1}{d_{hkl}^2} = \frac{h^2+k^2}{a^2} + \frac{l^2}{c^2} \quad (2)$$

In this regard, a and c represent the lattice constants, while d_{hkl} refers to the crystalline interplanar distance, which is calculated by Bragg's Law. Specifically, when applying this equation to the (002) diffraction peak, the equation simplifies to $c = 2 d_{hkl}$. The strain ε , along the c -axis is calculated by the equation (3) ³⁶-

$$\varepsilon = \frac{c-c_0}{c_0} \times 100\% \quad (3)$$

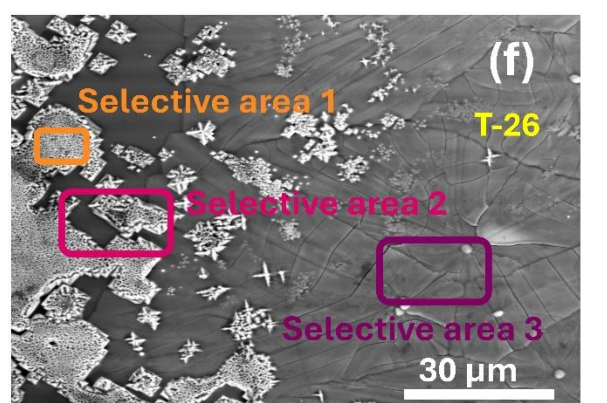
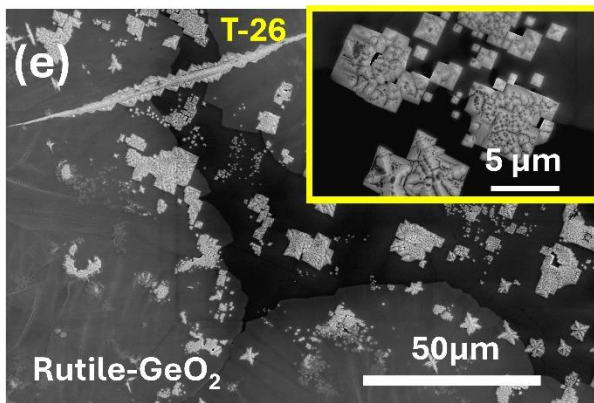
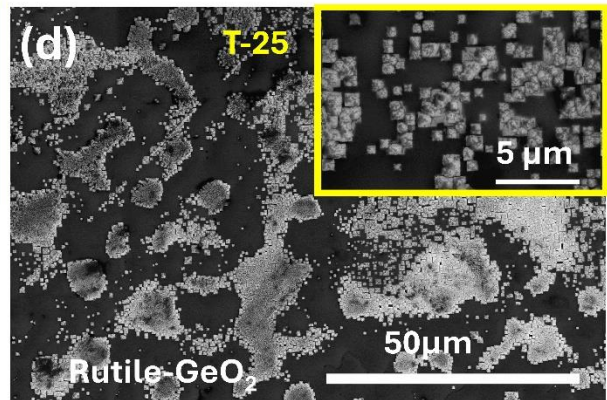
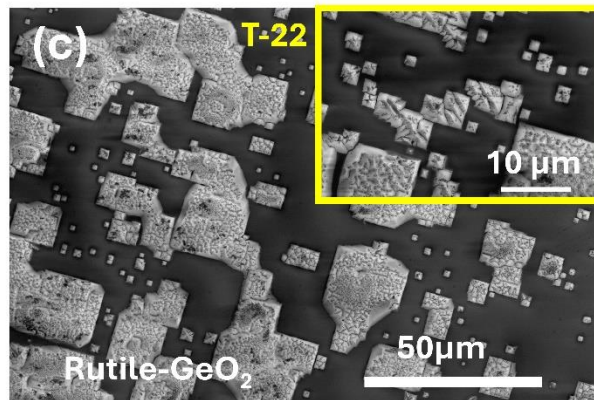
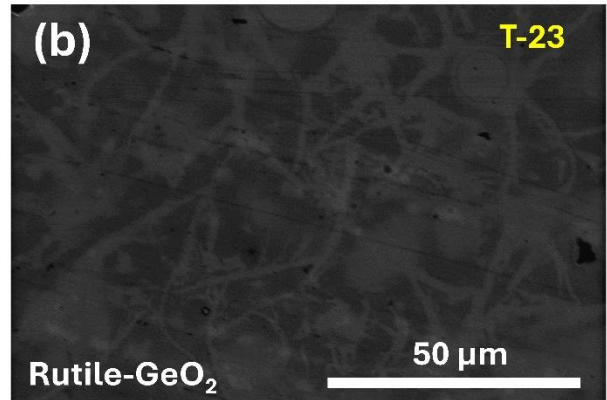
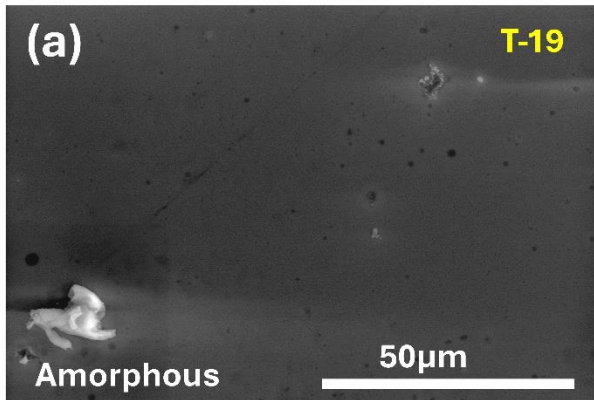
Where c_0 (2.86186 Å) is the unstrained c lattice parameter of r-GeO₂.³¹ Table III shows that the lattice constant c increases with higher growth temperatures, rotation speeds, and growth periods. Specifically, films grown at 840°C (T-23) have a lattice constant of 2.8552Å, which rises to 2.8687Å at 925°C (T-25) under the same conditions of 300 RPM and 90 min. Extending the growth period to 180 min (T-22) further increases the value to 2.8709Å. However, reducing the rotation speed to 170 RPM, sample T-26 exhibits a lattice constant of 2.8605 Å, closely matching the standard 2.86186 Å and showing a compressive strain of 0.048%. The variations in the lattice parameter c can be linked to several factors. At higher temperatures, increased atomic vibrations

due to enhanced thermal energy led to thermal expansion and potential alterations in defect densities, both of which can distort the lattice. At a moderate rotation speed of 170 RPM, optimal precursor distribution and sufficient atomic settling time promote uniform film growth. Conversely, too high a rotation speed might decrease the pressure, resulting in a shorter interaction time between precursors and the substrate. Consequently, the moderate rotation speed of 170 RPM produced films with lattice constants near standard values, indicating well-controlled growth conditions that stabilize the crystal structure. Moreover, the growth rate under mass transport-limited conditions is inversely related to the thickness of the boundary layer and varies with the rotation rate and operating pressure.³⁷ A higher growth rate with a thinner boundary layer at high rotation speed may negatively affect film quality.

Figures 4(a-h) and 5(a-f) depict SEM and AFM analyses of our films under various conditions. Sample T-19, grown at 725 °C, has a smooth surface as shown in Fig. 4(a). At 840 °C (T-23), the surface becomes rougher with visible irregular lines (Fig. 4(b)). AFM data show surface roughness of 3.13 nm for T-19 and 6.34 nm for T-23. At 925 °C, as indicated in Fig. 5(a) and (b). The surface of sample T-22 features distinct faceted crystals (Fig. 4(c)), and prolonged growth times lead to a larger, coalesced square pattern, leading to increased roughness of 181.8 nm (180 min, T-22) compared to ~99.52 nm for shorter periods (90 min, T-25) as shown in Fig. 5(c) and 5(d). In contrast, the surface morphology of sample T-26 with a lower susceptor rotation speed (170 RPM), depicted in Fig. 4(e), shows smaller roughness. The RMS roughness of T-26 is markedly improved to approximately 13 nm, as highlighted in Fig. 5(e). Figure 5(f) compares the RMS roughness of all the samples. The presence of a square pattern in the film raises questions about whether this is due to island growth or defects. To clarify this, EDX analysis was performed on three different regions as shown in Figure 4(f), with the chemical composition of these areas detailed in Fig. 4(g)

and the EDX mapping presented in Fig. 4(h). The comparison of SEM and EDX reveals that both the square-patterned and non-patterned regions exhibit similar ratios of Ge element content. It is worth noting that sample T-23, which lacks the square pattern, still demonstrates the crystalline properties of r-GeO₂, albeit of lower quality. These analyses indicate that the square patterns are more likely defects. However, for further confirmation, additional studies such as Transmission Electron Microscopy (TEM) could provide definitive evidence of the epitaxial nature of the film.

Although lower rotation speed here can improve the film quality, excessively low speeds should be avoided as they may lead to amorphous film formation, according to our recent findings.²⁹ According to classical nucleation theory, surface area scales with the square of the size (r^2) and volume scales with the cube (r^3) in three-dimensional systems. However, in thin films, both surface area and volume scale are similar to r^2 . This scaling suggests that interface energy plays a dominant role in shaping the morphology of the film. As a result, this energy influence is also likely responsible for the characteristic faceted or spherulitic patterns observed in different crystalline phases of GeO₂ films.



(g)

Element	Weight (%)	Atomic (%)
Selective area 1		
O K	26.2	61.3
Ge L	71.4	36.9
Ti K	2.4	1.9
Selective area 2		
O K	26.7	61.5
Ge L	68.5	34.8
Ti K	4.7	3.7
Selective area 3		
O K	26.3	61.3
Ge L	70.4	36.1
Ti K	3.3	2.5

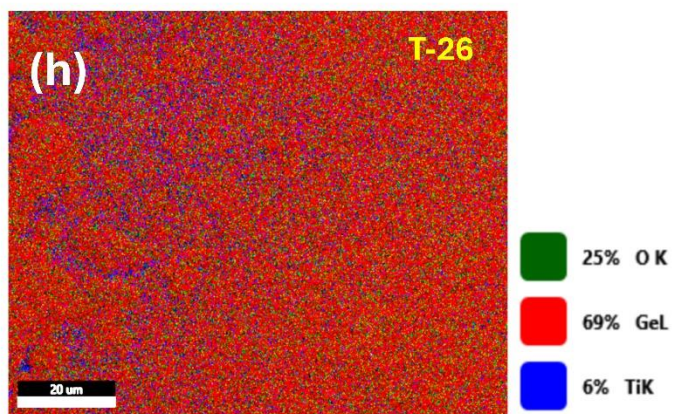


Figure 4. SEM images of r-GeO₂ films under various growth conditions: sample ID- (a) T-19, (b) T-23, (c) T-22, (d) T-25, and (e) T-26. Additional analyses for sample T-26 include (f) SEM image for chemical composition analysis, (g) corresponding EDX data for Fig (f), and (h) corresponding EDX mapping for Fig (f).

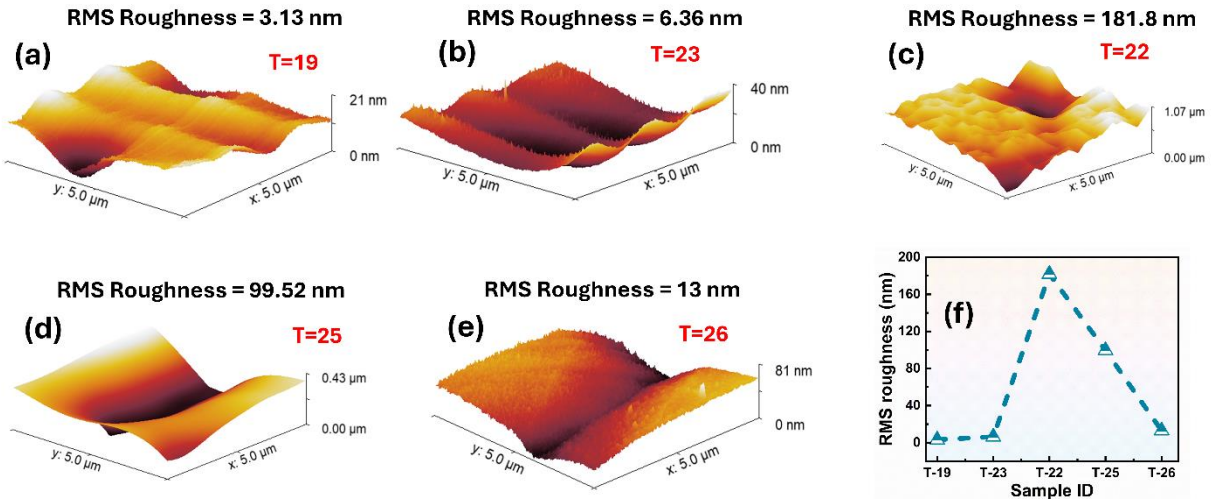


FIG. 5. Surface roughness by AFM of r-GeO₂ films at various growth conditions: (a) T-19, (b) T-23, (c) T-22, (d) T-25, and (e) T-26.

IV. Conclusion

In conclusion, our study has reported the successful growth of single crystal r-GeO₂ by MOCVD by investigating different growth parameters. The results affirm that the temperature of growth and rotation speed exert a profound influence on the crystalline quality of GeO₂ films. The growth temperature of 925 °C resulted in high-quality crystal films, while the low temperature of 725 °C resulted in amorphous based on the XRD results. However, longer growth at 925 °C makes both the crystal quality and surface morphology worse. By reducing the susceptor rotation speed to 170 RPM, both the epilayer crystal quality and surface roughness were improved, resulting in an FWHM of 0.181° and surface roughness of 13 nm. This comprehensive exploration provides a

foundational understanding for achieving a single crystal r-GeO₂ epilayer by MOCVD, helping to pave the way for the development of this new UWBG semiconductor.

AUTHOR DECLARATIONS

Conflict of Interest

The authors have no conflicts to disclose.

Author Contributions

Imteaz Rahaman: Data curation (lead); Formal analysis (lead); Investigation (lead); Methodology (lead); Bobby Duersch: Data curation (equal); Writing – review & editing (supporting), Formal analysis (supporting). Hunter D. Ellis: Writing – review & editing (supporting); Michael A. Scarpulla: Conceptualization (equal); Writing – review & editing (equal). Kai-Fu: Conceptualization (lead); Supervision (lead); Project administration (lead); Resources (lead).

DATA AVAILABILITY

The data that support the findings of this study are available from the corresponding authors upon reasonable request.

REFERENCES

¹ J.B. Casady, and R.W. Johnson, “Status of silicon carbide (SiC) as a wide-bandgap semiconductor for high-temperature applications: A review,” *Solid-State Electronics* **39**(10), 1409–1422 (1996).

² M. Yuan, Q. Xie, K. Fu, T. Hossain, J. Niroula, J.A. Greer, N. Chowdhury, Y. Zhao, and T. Palacios, “GaN Ring Oscillators Operational at 500 °C Based on a GaN-on-Si Platform,” *IEEE Electron Device Lett.* **43**(11), 1842–1845 (2022).

- ³ M. Feneberg, R.A.R. Leute, B. Neuschl, K. Thonke, and M. Bickermann, “High-excitation and high-resolution photoluminescence spectra of bulk AlN,” *Phys. Rev. B* **82**(7), 075208 (2010).
- ⁴ R. Sun, A.R. Balog, H. Yang, N. Alem, and M.A. Scarpulla, “Degradation of β -Ga₂O₃ Vertical Ni/Au Schottky Diodes Under Forward Bias,” *IEEE Electron Device Lett.* **44**(5), 725–728 (2023).
- ⁵ M. Xu, D. Wang, K. Fu, D.H. Mudiyansele, H. Fu, and Y. Zhao, “A review of ultrawide bandgap materials: properties, synthesis and devices,” *Oxford Open Materials Science* **2**(1), itac004 (2022).
- ⁶ B. Mallesham, S. Roy, S. Bose, A.N. Nair, S. Sreenivasan, V. Shutthanandan, and C.V. Ramana, “Crystal Chemistry, Band-Gap Red Shift, and Electrocatalytic Activity of Iron-Doped Gallium Oxide Ceramics,” *ACS Omega* **5**(1), 104–112 (2020).
- ⁷ K. Fu, S. Luo, H. Fu, K. Hatch, S.R. Alugubelli, H. Liu, T. Li, M. Xu, Z. Mei, Z. He, J. Zhou, C. Chang, F.A. Ponce, R. Nemanich, and Y. Zhao, “GaN-Based Threshold Switching Behaviors at High Temperatures Enabled by Interface Engineering for Harsh Environment Memory Applications,” *IEEE Trans. Electron Devices*, 1–5 (2023).
- ⁸ J.Y. Tsao, S. Chowdhury, M.A. Hollis, D. Jena, N.M. Johnson, K.A. Jones, R.J. Kaplar, S. Rajan, C.G. Van De Walle, E. Bellotti, C.L. Chua, R. Collazo, M.E. Coltrin, J.A. Cooper, K.R. Evans, S. Graham, T.A. Grotjohn, E.R. Heller, M. Higashiwaki, M.S. Islam, P.W. Juodawlkis, M.A. Khan, A.D. Koehler, J.H. Leach, U.K. Mishra, R.J. Nemanich, R.C.N. Pilawa-Podgurski, J.B. Shealy, Z. Sitar, M.J. Tadjer, A.F. Witulski, M. Wraback, and J.A. Simmons, “Ultrawide-Bandgap Semiconductors: Research Opportunities and Challenges,” *Adv Elect Materials* **4**(1), 1600501 (2018).

- ⁹ B. Chatterjee, K. Zeng, C.D. Nordquist, U. Singiseti, and S. Choi, “Device-Level Thermal Management of Gallium Oxide Field-Effect Transistors,” *IEEE Trans. Compon., Packag. Manufact. Technol.* **9**(12), 2352–2365 (2019).
- ¹⁰ S.J. Pearton, J. Yang, P.H. Cary, F. Ren, J. Kim, M.J. Tadjer, and M.A. Mastro, “A review of Ga₂O₃ materials, processing, and devices,” *Applied Physics Reviews* **5**(1), 011301 (2018).
- ¹¹ T. Kobayashi, T. Gake, Y. Kumagai, F. Oba, and Y. Matsushita, “Energetics and electronic structure of native point defects in α -Ga₂O₃,” *Appl. Phys. Express* **12**(9), 091001 (2019).
- ¹² Y. Zhang, Q. Su, J. Zhu, S. Koirala, S.J. Koester, and X. Wang, “Thickness-dependent thermal conductivity of mechanically exfoliated β -Ga₂O₃ thin films,” *Applied Physics Letters* **116**(20), 202101 (2020).
- ¹³ K.B. Nam, M.L. Nakarmi, J. Li, J.Y. Lin, and H.X. Jiang, “Mg acceptor level in AlN probed by deep ultraviolet photoluminescence,” *Applied Physics Letters* **83**(5), 878–880 (2003).
- ¹⁴ M.L. Nakarmi, K.H. Kim, M. Khizar, Z.Y. Fan, J.Y. Lin, and H.X. Jiang, “Electrical and optical properties of Mg-doped Al_{0.7}Ga_{0.3}N alloys,” *Applied Physics Letters* **86**(9), 092108 (2005).
- ¹⁵ M.W. Geis, T.C. Wade, C.H. Wuorio, T.H. Fedynyshyn, B. Duncan, M.E. Plaut, J.O. Varghese, S.M. Warnock, S.A. Vitale, and M.A. Hollis, “Progress Toward Diamond Power Field-Effect Transistors,” *Physica Status Solidi (a)* **215**(22), 1800681 (2018).
- ¹⁶ M. Stapelbroek, and B.D. Evans, “Exciton structure in the u.v.-absorption edge of tetragonal GeO₂,” *Solid State Communications* **25**(11), 959–962 (1978).
- ¹⁷ S. Chae, J. Lee, K.A. Mengle, J.T. Heron, and E. Kioupakis, “Rutile GeO₂: An ultrawide-band-gap semiconductor with ambipolar doping,” *Applied Physics Letters* **114**(10), 102104 (2019).

- ¹⁸ K.A. Mengle, S. Chae, and E. Kioupakis, “Quasiparticle band structure and optical properties of rutile GeO₂, an ultra-wide-band-gap semiconductor,” *Journal of Applied Physics* **126**(8), 085703 (2019).
- ¹⁹ K. Bushick, K.A. Mengle, S. Chae, and E. Kioupakis, “Electron and hole mobility of rutile GeO₂ from first principles: An ultrawide-bandgap semiconductor for power electronics,” *Applied Physics Letters* **117**(18), 182104 (2020).
- ²⁰ S. Chae, K. Mengle, K. Bushick, J. Lee, N. Sanders, Z. Deng, Z. Mi, P.F.P. Poudeu, H. Paik, J.T. Heron, and E. Kioupakis, “Toward the predictive discovery of ambipolarly dopable ultra-wide-band-gap semiconductors: The case of rutile GeO₂,” *Applied Physics Letters* **118**(26), 260501 (2021).
- ²¹ S. Chae, K.A. Mengle, R. Lu, A. Olvera, N. Sanders, J. Lee, P.F.P. Poudeu, J.T. Heron, and E. Kioupakis, “Thermal conductivity of rutile germanium dioxide,” *Applied Physics Letters* **117**(10), 102106 (2020).
- ²² C.A. Niedermeier, K. Ide, T. Katase, H. Hosono, and T. Kamiya, “Shallow Valence Band of Rutile GeO₂ and P-type Doping,” *J. Phys. Chem. C* **124**(47), 25721–25728 (2020).
- ²³ J.W. Goodrum, “Top-seeded flux growth of tetragonal GeO₂,” *Journal of Crystal Growth* **7**(2), 254–256 (1970).
- ²⁴ S. Kawasaki, O. Ohtaka, and T. Yamanaka, “Structural change of GeO₂ under pressure,” *Phys Chem Minerals* **20**(8), 531–535 (1994).
- ²⁵ V.V. Brazhkin, A.G. Lyapin, R.N. Voloshin, S.V. Popova, E.V. Tat’yanin, N.F. Borovikov, S.C. Bayliss, and A.V. Sapelkin, “Pressure-Induced Crossover between Diffusive and Displacive Mechanisms of Phase Transitions in Single-Crystalline α - G e O 2,” *Phys. Rev. Lett.* **90**(14), 145503 (2003).

- ²⁶ S. Chae, H. Paik, N.M. Vu, E. Kioupakis, and J.T. Heron, “Epitaxial stabilization of rutile germanium oxide thin film by molecular beam epitaxy,” *Applied Physics Letters* **117**(7), 072105 (2020).
- ²⁷ H. Takane, and K. Kaneko, “Establishment of a growth route of crystallized rutile GeO₂ thin film ($\geq 1 \mu\text{m/h}$) and its structural properties,” *Applied Physics Letters* **119**(6), 062104 (2021).
- ²⁸ G. Deng, K. Saito, T. Tanaka, M. Arita, and Q. Guo, “Pulsed laser deposition growth of ultra-wide bandgap GeO₂ film and its optical properties,” *Applied Physics Letters* **119**(18), 182101 (2021).
- ²⁹ I. Rahaman, H.D. Ellis, K. Anderson, M.A. Scarpulla, and K. Fu, “Growth of GeO₂ on *R*-Plane and *C*-Plane Sapphires by MOCVD,” *ACS Appl. Eng. Mater.*, acaenm.4c00320 (2024).
- ³⁰ S. Chae, L.A. Pressley, H. Paik, J. Gim, D. Werder, B.H. Goodge, L.F. Kourkoutis, R. Hovden, T.M. McQueen, E. Kioupakis, and J.T. Heron, “Germanium dioxide: A new rutile substrate for epitaxial film growth,” *Journal of Vacuum Science & Technology A* **40**(5), 050401 (2022).
- ³¹ A.A. Bolzan, C. Fong, B.J. Kennedy, and C.J. Howard, “Structural Studies of Rutile-Type Metal Dioxides,” *Acta Crystallogr B Struct Sci* **53**(3), 373–380 (1997).
- ³² M. Higashiwaki, K. Sasaki, A. Kuramata, T. Masui, and S. Yamakoshi, “Gallium oxide (Ga₂O₃) metal-semiconductor field-effect transistors on single-crystal β -Ga₂O₃ (010) substrates,” *Applied Physics Letters* **100**(1), 013504 (2012).
- ³³ S.J. Pearton, J. Yang, P.H. Cary, F. Ren, J. Kim, M.J. Tadjer, and M.A. Mastro, “A review of Ga₂O₃ materials, processing, and devices,” *Applied Physics Reviews* **5**(1), 011301 (2018).
- ³⁴ S. Chae, K. Mengle, K. Bushick, J. Lee, N. Sanders, Z. Deng, Z. Mi, P.F.P. Poudeu, H. Paik, J.T. Heron, and E. Kioupakis, “Toward the predictive discovery of ambipolarly dopable ultra-wide-

band-gap semiconductors: The case of rutile GeO₂,” *Applied Physics Letters* **118**(26), 260501 (2021).

³⁵ W.D. CALLISTER JR, *MATERIALS SCIENCE AND ENGINEERING: An Introduction* (WILEY, S.I., 2020).

³⁶ R. Ghosh, D. Basak, and S. Fujihara, “Effect of substrate-induced strain on the structural, electrical, and optical properties of polycrystalline ZnO thin films,” *Journal of Applied Physics* **96**(5), 2689–2692 (2004).

³⁷ B. Mitrovic, A. Gurary, and W. Quinn, “Process conditions optimization for the maximum deposition rate and uniformity in vertical rotating disc MOCVD reactors based on CFD modeling,” *Journal of Crystal Growth* **303**(1), 323–329 (2007).